

Sieber, M., Wilke, F., Koch-Müller, M. (2020):
Partition Coefficients of Trace Elements Between
Carbonates and Melt and Suprasolidus Phase
Relation of Ca-Mg-Carbonates at 6 Gpa. -
American Mineralogist, 105, 6, 922-933.

<https://doi.org/10.2138/am-2020-7098>

1 **FINAL - DRAFT**

2 **PARTITION COEFFICIENTS OF TRACE ELEMENTS BETWEEN CARBONATES AND**
3 **MELT AND SUPRASOLIDUS PHASE RELATION OF CA-MG-CARBONATES AT**
4 **6 GPa**

5 Sieber Melanie J.^{1*}, Wilke Franziska D. H.¹, Koch-Müller Monika¹

6 ¹ GFZ German Research Centre for Geosciences, Section 3.6 and 3.1, Telegrafenberg, 14473

7 Potsdam, Germany

8 *corresponding author: E-mail address: sieber@gfz-potsdam.de

9 **Abstract**

10 The presence of Ca-Mg-carbonates affects the melting and phase relations of peridotites and
11 eclogites in the mantle and (partial) melting of carbonates liberates carbon from the mantle to
12 shallower depths. The onset and composition of incipient melting of carbonated peridotites
13 and carbonated eclogites are influenced by the pure CaCO₃-MgCO₃-system making
14 understanding of the phase relations of Ca-Mg-carbonates fundamental in assessing carbon
15 fluxes in the mantle. By performing high pressure and temperature experiments, this study
16 clarifies the suprasolidus phase relations of the nominally anhydrous CaCO₃-MgCO₃-system
17 at 6 GPa showing that Ca-Mg-carbonates will (partially) melt for temperatures above
18 ~1300 °C. A comparison with data from thermodynamic modelling confirms the
19 experimental results. Furthermore, partition coefficients for Li, Na, K, Sr, Ba, Nb, Y and rare
20 earth elements between calcite and dolomitic melt, Ca-magnesite and dolomitic melt and
21 magnesite and dolomitic melt are established.

22 Experiments were performed at 6 GPa and between 1350 to 1600 °C utilizing a rotating
23 multi-anvil press. Rotation of the multi-anvil press is indispensable to establish equilibrium
24 between solids and carbonate liquid. Major and trace elements were quantified with EPMA
25 and LA-ICP-MS, respectively.

26 The melting temperature and phase relations of Ca-Mg-carbonates depend on the
27 Mg/Ca-ratio. For instance, Ca-rich carbonates with a molar Mg/(Mg+Ca)-ratio (X_{Mg}) of 0.2
28 will transform into a dolomitic melt ($X_{Mg}=0.33-0.31$) and calcite crystals ($X_{Mg}=0.19-0.14$) at
29 1350-1440 °C. Partial melting of Mg-rich carbonates ($X_{Mg}=0.85$) will produce a dolomitic
30 melt ($X_{Mg}=0.5-0.8$) and Ca-bearing magnesite ($X_{Mg}=0.89-0.96$) at 1400-1600 °C. Trace
31 element distribution into calcite and magnesite seems to follow lattice constraints for divalent
32 cations. For instance, the compatibility of calcite ($X_{Mg}=0.14-0.19$) for Sr and Ba decreases as
33 the cation radii increases. Ca-Mg-carbonates are incompatible for rare earth elements (REEs),
34 whereby the distribution between carbonates and dolomitic melt depends on the Mg/Ca ratio
35 and temperature. For instance, at 1600 °C, partition coefficients between magnesite
36 ($X_{Mg}=0.96$) and dolomitic melt ($X_{Mg}=0.8$) vary by two orders of magnitudes from 0.001 to
37 0.1 for light-REEs to heavy-REEs. In contrast, partition coefficients of REEs (and Sr, Ba, Nb
38 and Y) between magnesite ($X_{Mg}=0.89$) and dolomitic melt ($X_{Mg}=0.5$) are more uniform
39 scattering marginal between ~0.1-0.2 at 1400 °C.

40 **Keywords**

41 Melt relations of carbonates at 6 GPa (~200 km)

42 Deep carbon cycle

43 Trace element partitioning

44 Carbonate stability in the mantle

45 **Introduction**

46

47 Ca-Mg-carbonates ((Ca,Mg)CO₃) are introduced into the mantle at subduction zones, while
48 volcanic eruption outgases carbon back to the lithosphere and atmosphere (Hazen et al.
49 2013). Within the subducting slab, carbonates are most abundant in sediments and in the

50 hydrothermally altered parts of the oceanic crust (Alt and Teagle 1999). During heating and
51 compression, some carbon is released from the subducting lithologies by decomposition and
52 devolatilisation into a mobile phase (fluid or melt). Carbonic fluids eventually return to the
53 surface via arc related magmatism and by diffuse outgassing (Hazen et al. 2013; Kelemen
54 and Manning 2015) or may interact with (hydrated) peridotites in the subducting slab and
55 with the supra-subduction mantle to form Ca-Mg-carbonates (Piccoli et al. 2016; Scambelluri
56 et al. 2016; Sieber et al. 2018). However, in the absence of water, carbonates are stable along
57 typical subduction zone geotherms. Therefore, carbonate bearing lithologies in the slab that
58 do not experience pervasive dehydration or fluid infiltration can transport carbonates to
59 greater mantle depths (Gorman et al. 2006; Kerrick and Connolly 1998; Kerrick and
60 Connolly 2001). The presence of some carbonates in the mantle is evidenced, for instance, by
61 carbonate-bearing ultra-high pressure metamorphic rocks (Korsakov and Hermann 2006;
62 Shatsky et al. 2006), carbonate-bearing mantle xenoliths (Ionov et al. 1993; Ionov et al. 1996)
63 and inclusions in diamonds (Stachel and Harris 2008; Wang et al. 1996).

64 Experimental studies demonstrate the stability of carbonates at the solidus of carbonated
65 peridotites and eclogites and flag the relevance of carbonates to their melt relations and
66 melting temperature (Brey et al. 2008; Dasgupta et al. 2004; Yaxley and Green 1994). For
67 instance, the mantle solidus is reduced from ~1730 °C to ~1250-1380 °C at 6 GPa in the
68 presence of carbonates (Dalton and Presnall 1998; Dasgupta and Hirschmann 2010;
69 Hirschmann 2000). Even small amounts of carbonates can incite melting of peridotites,
70 whereby carbonates are completely consumed to form dolomitic melts according to the
71 approximate reaction of 2MgCO_3 (magnesite) + $\text{CaMgSi}_2\text{O}_6$ (clinopyroxene) = $\text{CaMg}(\text{CO}_3)_2$
72 (liquid) + $\text{Mg}_2\text{Si}_2\text{O}_6$ (orthopyroxene) (Dalton and Presnall 1998). Low-degree melting of a
73 carbonated mantle produces CO_2 -rich melts which are potentially the precursor of
74 carbonatites and kimberlites (Dalton and Wood 1993; Kruk et al. 2018; Yaxley and Brey

75 2004). The presence of CO₂-rich melts may contribute to the low electrical conductivity of
76 the asthenosphere (Gaillard et al. 2008).

77 The composition of the incipient melt from partial melting of carbonated peridotites and
78 carbonated eclogites is influenced by the melt relations of the pure CaCO₃-MgCO₃-system
79 (Dalton and Presnall 1998; Dasgupta and Hirschmann 2006; Yaxley and Brey 2004). Thus,
80 the melting point and suprasolidus phase relations of carbonates are fundamental in assessing
81 carbon fluxes in the mantle. Despite the mentioned relevance of Ca-Mg-carbonates, their
82 liquidus and suprasolidus phase relations remain controversial. Comparison of recent
83 experimental studies reveals an offset of ~100-200 °C for the nominally anhydrous liquidus at
84 6 GPa (Buob et al. 2006; Müller et al. 2017; Shatskiy et al. 2018). This discrepancy is critical
85 for the onset and degree of melting. For instance, at 6 GPa and between ~1300 and 1400 °C
86 carbonates will either melt over a wide compositional range of Ca_{0.1-0.9}Mg_{0.9-0.1}CO₃ (Müller
87 et al. 2017) or will be stable (Shatskiy et al. 2018). By performing high pressure and
88 temperature experiments, this study clarifies the suprasolidus phase relations of
89 Ca-Mg-carbonates at 6 GPa and compares the results to thermodynamic modelling of the
90 CaCO₃-MgCO₃-system and to previous experimental studies.

91 Carbonate-rich melts are superb metasomatic agents, because they are buoyant with respect
92 to peridotites, show high solubility for other volatiles (e.g. H₂O) and can be enriched in trace
93 elements (Dalton and Wood 1993; Keppler 2003). Since the incipient melts of carbonated
94 peridotites and carbonated eclogites are influenced by the pure carbonate-system, the trace
95 element signature of near solidus, CO₂-rich liquids might also be influenced by the
96 distribution of trace elements between carbonates and CO₂-rich melts. Thus, this study
97 provides, for the first time, partition coefficients of Li, Na, K, Sr, Ba, Nb, Y and rare earth
98 elements between calcite and dolomitic melt and magnesite and dolomitic melt at 6 GPa.

Experimental methods

99
100 Two starting mixtures containing natural magnesite ($\text{Mg}_{29.6}\text{Fe}_{0.2}\text{Mn}_{0.1}\text{Ca}_{0.1}(\text{CO}_3)_{10}$ from
101 Brumado, Brazil) and synthetic CaCO_3 regulating $X_{\text{Mg}} = \frac{n_{\text{MgCO}_3}[\text{mol}]}{n_{\text{MgCO}_3}[\text{mol}] + n_{\text{CaCO}_3}[\text{mol}]}$ to 0.85
102 (CM1) and 0.2 (CM2) were used in multi-anvil experiments (Table 1). Starting mixtures
103 (CM1 and CM2) were doped with laboratory grade Li-, Na-, K-, Ba- and Sr-carbonate and
104 Pb-, Nb- Y-oxides and rare earth elements (REEs) as oxides (purities $\geq 99.9\%$; expect for
105 La_2O_3 with a purity of 94%). All starting mixtures were ground in acetone for ~ 0.5 h and
106 dried at $\sim 120^\circ\text{C}$ for >48 h before loading into cold-sealed Pt-capsules. Pt-capsules had an
107 outer height and diameter of 3 mm and 2 mm, respectively, and a wall thickness of 0.2 mm.
108 An 18/11-assembly and a stepped graphite heater, minimizing the temperature (T) gradient
109 across the capsule (Walter et al. 1995), were employed. Assembled octahedrons were stored
110 at $\sim 120^\circ\text{C}$ until conducting the experiment. Using the same assembly and multi-anvil
111 apparatus, the absence of a T-gradient and a T-accuracy within 1% at 1500°C was verified
112 previously by applying the two-pyroxene geothermometer (Müller et al. 2017). Temperature
113 was monitored over the run duration of 6 h with a Type C thermocouple
114 (WRe5%-WRe26%-wires) surrounded by BN-powder to establish reduced conditions
115 preventing a temporal drift of the measured temperature (Watenphul et al. 2009). The
116 thermocouple failed in run A and temperature was controlled by the heating power.
117 Experiments were conducted at 6 GPa, between 1350 to 1600°C for 6 h in a Walker style
118 multi-anvil apparatus. To encourage equilibrium between melt and crystals, the press was
119 continuously rotated by 180° around its axis with $5^\circ/\text{sec}$ and rotation was started before
120 heating. The steady rotation was stopped to separate melt and crystals within $\lesssim 30$ sec before
121 quenching.

122 **Methods**

123 **Analytical Methods**

124 After the multi-anvil experiments, the recovered capsules were mounted, polished and
125 C-coated for Electron Probe Micro Analyzes (EPMA). Quantitative wavelength dispersive
126 spectrometry (WDS) was performed on a JEOL Superprobe JXA-8230 and a JEOL
127 Hyperprobe JXA-8500F. For accurate quantification of Mg, Ca, Fe, Mn, Ba and Sr in
128 carbonates, an acceleration voltage of 15 kV, a beam current of 1-10 nA, a probe size of
129 5-40 μm and relative short measurement times between 30 to 70 sec (for background and
130 peak) were applied. Those analytical parameters are reported as optimal for precise electron
131 probe micro-analyzes of carbonates (Zhang et al. 2017). To analyze melt-pockets in run D
132 (Figure 1d, h), the size of the electron beam needed to be reduced to 1 μm . PRZ-matrix
133 correction was applied and various carbonate standards were analyzed during the course of
134 the analytical sessions to ensure the quality of measured data.

135 Afterwards, the trace element composition was determined by LA-ICP-MS (Laser Ablation -
136 Inductively Coupled Plasma - Mass Spectrometry) using a Geolas Compex Pro 193 nm
137 excimer laser coupled to a Thermo iCAP triple quad ICP-MS. The laser was operated with a
138 frequency of 10 Hz and energy of 140 mNm. The diameter of the round laser spot ranged
139 between 16 to 44 μm . Analyzes took place near the EPMA positions and Ca was used as
140 reference element for quantification. NIST 610 was selected as the calibration standard and
141 NIST 612 and Macs3 Ca-carbonate served as secondary standards for quality control.
142 Reference values were taken from Jochum et al. (2011) and [http://georem.mpch-
143 mainz.gwdg.de](http://georem.mpch-mainz.gwdg.de). For data processing, the software Iolite was applied.

144 Raman measurements were performed to confirm the absence of hydrous phases using a
145 HORIBA Jobin Yvon LabRAM HR800 VIS spectrometer with a DPSS laser of 405 and

146 473 nm wavelength. The spectral ranges were 100-1200 cm^{-1} and 3000-4000 cm^{-1} and the
147 data acquisition time ranged from 10 to 30 sec.

148 **Phase proportions and thermodynamic model**

149 To calculate the mass proportions of solid carbonates and carbonate melts for each
150 experiment, first the volume of carbonates and melt was obtained from geometrical
151 constraints and then the density of solid carbonates was computed for conversion into mass%.
152 In run A and B the volume of the melt was calculated from averaging the area of the
153 semicircles in which the melt occurs (Figure 1a, b) and assuming the semicircle continues
154 around the whole, inner capsule wall. Solid carbonates fill then the rest of the total, inner
155 capsule volume. For simplification, the capsule volume prior to the experiment was used.
156 Consequently, the obtained proportions of melts are slightly underestimated and the
157 proportions of solid carbonates are somewhat overestimated. To obtain the volume of
158 carbonate crystals in run C, we assumed the solid fraction occurs in a half-ball at the top of
159 the capsule and in a half-ball plus cylinder at the bottom of the capsule. For run D, the
160 software ImageJ was used to compute the area proportion of melt and solids from the contrast
161 difference in BSE-images.

162 For conversion into mass proportions (listed in Table 1), the total weight of the system and
163 the density of solid carbonates were needed. The latter was computed at run PT-conditions
164 with *Perple_X* (Connolly 2005) using the Holland and Powell (1998) data base as revised by
165 the authors in 2002. In the calculations the solid solution model for carbonates after Franzolin
166 et al. (2011) was applied. The calibration of this solid solution bases upon subsolidus piston-
167 cylinder experiments performed in the CaCO_3 - MgCO_3 - FeCO_3 system at 3.5 GPa and 900-
168 1100 °C.

169 The error on the calculated phase proportions was not quantified, but uncertainties in the
170 geometrical obtained volume proportions (e.g. the inner volume of the capsule prior to the

171 experiment), the computed densities (extrapolation from data based on experiment at lower
172 PT) and measured compositions may contribute to the error.

173 **Results**

174 **Textures and phase assemblages**

175 In all experiments, a solid and liquid phase was present under high pressure (P) and
176 temperature (T). In BSE-images, liquids are identified by a dendritic habitus which is typical
177 for quenched carbonate melts (Vernon 2004). In contrast, carbonates crystallized during the
178 experiment are coarser grained and have sharp, regular crystal forms. Throughout the text, the
179 terms ‘melt’ and ‘solid’ will refer to the state of the matter under high PT. Solid carbonates
180 are magnesite crystals in experiments using CM1. In experiments using CM2, Raman
181 spectroscopy implies Mg-bearing calcite as solid carbonate, but disordered carbonate could
182 also appear (Buob et al. 2006).

183 Carbonate crystals and carbonate melt are spatially separated in run A, B and C, whereby
184 melt occurs in pools centered in the middle of the Pt-capsule and solids occur on both ends of
185 the capsule in a semicircle reminding on an hourglass (Figure 1a, b, c). In run D, melt occurs
186 interstitial between magnesite crystals with a diameter $\lesssim 10 \mu\text{m}$ (Figure 1d, h). Calcite
187 crystals are larger grained with diameters up to $\lesssim 0.5 \text{ mm}$ and show cleavage planes (run A,
188 run B). In run A, small amounts of periclase crystals occur within melt pools and surrounded
189 by calcite grains at the rims of the capsule (Figure 1e). Degassing of the melt upon quenching
190 may have triggered the formation of periclase, or small amounts of periclase were present as
191 inclusions in the natural magnesite used in the starting mixtures.

192 For each experiment, the proportions of the solid and liquid phase were constrained from
193 geometric observations and using computed densities of solid carbonates (for details on the
194 mass-balance calculations the reader is referred to the Methods section). The phase

195 proportions depend on the bulk composition and increase with temperature (Table 1). Using
196 the obtained phase proportions (Table 1) and measured compositions, X_{Mg} of the bulk system
197 was calculated and is consistent within a deviation of ~1.5% to ~5% to X_{Mg} of the starting
198 mixtures. This demonstrates that the obtained proportions are reliable and implies equilibrium
199 since the lever ruler is fulfilled.

200 **Figure 1**

201 **Major element compositions**

202 Ca-magnesite with $X_{Mg}=0.89$ (run D) and magnesite with $X_{Mg}=0.96$ (run C) are formed in
203 experiments using starting mixture CM1 (Table 1). Note that, ‘Ca-magnesite’ and
204 ‘magnesite’ will be used to refer to magnesite with $X_{Mg}=0.89$ and $X_{Mg}=0.96$, respectively.
205 Using CM2 in run A and run B, calcite crystals with X_{Mg} of 0.14 and 0.19 are formed
206 (Table 1). Within a single experiment, the major (and trace) element composition of
207 carbonates is homogeneous and uniform across the capsule. Only in run B, two small
208 ($\leq 50 \mu m$) calcite grains at the bottom of the capsule with $X_{Mg}=0.28$ differ compositionally
209 from the overall calcite composition ($X_{Mg}=0.19$).

210 To constrain the major and minor element composition of the melt, EPMA analyses were
211 performed with a beam size of 20-40 μm , which exceeds the size of dendritic carbonate
212 crystals (Figure 1e-g). The beam size was reduced to 1 μm to analyze the melt composition in
213 run D (Figure 1h). All melts are dolomitic with X_{Mg} ranging between 0.5 to 0.8 for
214 experiments performed with CM1 (run D, C) and between 0.31 to 0.33 for experiments
215 performed with CM2 (run A, B; Table 1).

216 **Table 1**

217 **Trace elements and partition coefficients**

218 With LA-ICP-MS we determined the trace element composition of carbonates and melt
219 except for run D where melt-pools are so small (Figure 1h) that several analyzes were

220 contaminated by neighbouring carbonate grains. Additionally to LA-ICP-MS, the
221 concentrations of Mn, Fe, Ba and Sr were determined by EPMA for all phases. The EPMA
222 results correlate well with concentrations obtained by LA-ICP-MS (Figure 2). Also, the trace
223 element concentration of the melt was constrained from mass-balance calculations. Hereby,
224 the trace element content in the melt is calculated from the known concentrations in the
225 starting materials, the measured concentrations in carbonates and using the proportions of
226 melt and carbonates listed in Table 1. The measured trace element content of the melt
227 corresponds, within the uncertainty, to the calculated concentrations (Figure 2). Thus, the
228 mass-balance approach is suitable to constrain the trace element concentration in run D.

229 **Figure 2**

230 Normalizing the trace element concentrations to the starting material demonstrates that Li,
231 Na, K, Nb and most REEs are enriched in the melt (Figure 3). The mass-balance approach
232 cannot be applied for elements forming alloys with the Pt of the capsule, because the bulk
233 amount is overestimated. Elements like Mn, Fe, Pb, Pr, Gd and Tb which are depleted in
234 carbonate grains and the melt of the same experiment, may have formed alloys with the Pt of
235 the capsule assuming the composition of the starting mixture is well defined.

236 **Figure 3**

237 Partition coefficients for Li, Na, K, Sr, Ba, Nb, Y and REEs (except Pr, Gd and Tb) between
238 magnesite, Ca-magnesite or calcite and dolomitic melt have been established. Assuming trace
239 elements (*i*) obey Henry's law, the partition coefficient (*D*) can be defined as quotient of the
240 concentration of an element in the solid-carbonate (c_i^s) and its concentration in the liquid
241 phase (c_i^l).

$$242 \quad D_i^{s-l} = \frac{c_i^s}{c_i^l}$$

243 Sr and Ba are moderately incompatible in calcite with *D* ranging from 0.63 ± 0.05 to 0.8 ± 0.2
244 and from 0.14 ± 0.05 to 0.26 ± 0.07 (run A, B; Table 2). Single charged Li, Na and K are

245 incompatible in calcite with D ranging from 0.03 to 0.3 (Table 2). Trivalent Y and REEs are
246 moderately incompatible in calcite with D between 0.2 and 0.3, whereby LREEs (La, Ce, Nd,
247 Sm) are slightly less compatible compared to HREEs (Eu, Dy, Ho, Er, Tm, Yb, Lu, Y)
248 (classification of REEs taken from the Geological-Society-London (2011)). Nb is
249 incompatible in calcite with $D \lesssim 0.002$.

250 Li, Na and K are incompatible in magnesite and strongly enriched in the dolomitic melt.
251 Partitioning coefficients of Sr, Ba, Y, REEs and Nb between Ca-magnesite ($X_{Mg}=0.89$) and
252 dolomitic melt ($X_{Mg}=0.5$) at 1400 °C are between ~0.1 and 0.2 (run D; Table 2). The partition
253 coefficients between magnesite ($X_{Mg}=0.96$) and dolomitic melt ($X_{Mg}=0.8$) at 1600 °C increase
254 continuously from ~0.001 to ~0.1 between LREEs and HREEs (run C; Table 2). Similar, the
255 compatibility of magnesite for Sr and Ba decreases with decreasing Ca content and increasing
256 temperature (Table 2). For instance, the partition coefficient of Sr between Ca-magnesite
257 ($X_{Mg}=0.89$) and dolomitic melt ($X_{Mg}=0.5$) is ~0.1 at 1400 °C (run D) but is reduced to
258 0.009 ± 0.001 as Ca in magnesite decreases to $X_{Mg}=0.96$ at 1600 °C (run C).

259 **Table 2**

260 **Discussion**

261 By performing high PT-experiments, this study resolves the suprasolidus phase relations of
262 Ca-Mg-carbonates at 6 GPa and determines trace element partition coefficients between
263 calcite, Ca-magnesite or magnesite and dolomitic melt. In the discussion, first the approach to
264 equilibrium will be considered. Then, the obtained suprasolidus phase relations will be
265 compared to recent literature and thermodynamic modelling and, finally, the trace element
266 partition coefficients will be discussed.

267 **Approach to equilibrium**

268 Multiple lines of evidence support equilibrium established during the experiment. The
269 absence of compositional zoning in all experiments supports chemical equilibrium. In all
270 experiments carbonates are homogeneous in their major and trace element composition as
271 evidenced by EPMA and LA-ICP-MS profiles. Equilibrium is further supported by the
272 applicability of the lever rule and by the good correlation of the liquidus between our
273 experiments and the thermodynamic modelling (see next section and Figure 4b). The
274 multi-anvil press was rotated throughout the entire run duration (stopping the rotation
275 $\lesssim 30$ sec before quenching) enhancing equilibrium between solids and a mobile phase
276 (Schmidt and Ulmer 2004). Except for run D, liquid and solids are sequestered after the
277 experiment. Limited interconnectivity and the relative small melt proportion in run D may
278 have hampered the spatial separation of the liquid and carbonate crystals. In run D
279 melt-pockets occur in triple-junctions between homogenous Ca-magnesite crystals suggesting
280 equilibrium (Hunter and McKenzie 1989). The ‘hourglass’ texture in run A, B and C, with
281 solids in a semicircle on both ends of the capsule and the liquid phase in the middle, has
282 previously been reported for fluid saturated systems (Deon et al. 2011). This hourglass
283 texture might be due to a small thermal gradient with the hottest part in the centre of the
284 capsule. Nonetheless, the absence of a temperature gradient has previously been verified for
285 the same experimental set-up by applying the two-pyroxene system as an internal
286 thermometer (see Figure 3 in Müller et al. (2017)). Adhesive and/or centrifugal forces may
287 have fostered the development of the hourglass texture during rotation. In any case, Müller et
288 al. (2017) demonstrated that a hydrous, CO₂-rich fluid and carbonates are intermingled when
289 the experiment is quenched during rotation of the multi-anvil press (their Figures 6 a-c).
290 Thus, they concluded that the mobile phase first separates from the solid phase when the
291 rotation is stopped.

292 **Suprasolidus phase relations**

293 Suprasolidus phase relations depend on the bulk composition and are controlled either by the
294 Ca-rich or Mg-rich part relative to the peritectic point (P1, Figure 4). Experimental studies
295 constrained the peritectic point at 6 GPa to $X_{Mg} \sim 0.35-0.5$ and 1300-1400 °C, but report an
296 offset of up to ~ 120 °C for the liquidus temperature of Ca-rich carbonates and a larger
297 discrepancy in temperature of up to ~ 200 °C for Mg-rich carbonates (Buob 2003; Buob et al.
298 2006; Müller et al. 2017; Shatskiy et al. 2018). This T-discrepancy is particularly crucial
299 since it affects the onset and extent of melting assuming a mantle temperature of
300 1375-1490 °C at ~ 200 km (Ita and Stixrude 1992; McKenzie et al. 2005). For instance, at
301 1375 °C, Ca-Mg-carbonates may either be stable or may completely melt over a
302 compositional range of $0.2 \lesssim X_{Mg} \lesssim 0.5$ (Müller et al. 2017; Shatskiy et al. 2018). Because of
303 this discrepancy in the suprasolidus phase relations, key experiments were performed
304 unravelling that carbonates will melt at 6 GPa for temperatures above ~ 1300 °C.

305 Melting was evidenced in all experiments by the presence of a liquid and crystalline phase.
306 The median composition of solid carbonates and carbonate melt is plotted in Figure 4 and the
307 error represents the complete analytical range (minimum to maximum) without outlier
308 rejection. In comparison to previous, experimental studies by Müller et al. (2017) and
309 Shatskiy et al. (2018), the here reported suprasolidus phase relations are complementary for
310 compositions Ca-richer to the peritectic point and intermediate for Mg-richer compositions
311 (Figure 4a). Buob (2003) and Buob et al. (2006) are not considered for a direct comparison,
312 because they report quench problems and thus extrapolated the liquidus curve for the Mg-rich
313 side based on two experiments performed below 1400 °C. Differences in the experimental
314 results could be caused by a T-gradient in the capsule and the hygroscopic nature of the
315 starting materials. Further, redox conditions and errors in quantification of the composition of
316 run products may contribute to the different results. A T-gradient is unavoidable in high PT

317 experiments, but can be reduced by using a stepped graphite heater (Walter et al. 1995), as
318 employed in this study. Using the same experimental set-up, a homogenous temperature
319 distribution, within $\pm 1\%$ at 6 GPa and 1500 °C, was verified utilizing the two pyroxene
320 thermometer (Müller et al. 2017). The presence of even small amounts of water likely
321 reduces the solidus. Buob (2003), Buob et al. (2006), Müller et al. (2017), Shatskiy et al.
322 (2018) and this study, all used ground carbonates in the starting mixes, which are hygroscopic
323 and thus may adsorb some water from the atmosphere. Care was taken to minimize addition
324 of water by storing the starting mixtures above 100 °C. Müller et al. (2017) reported the
325 formation of minor amounts of brucite in their experiments indicating the presence of some
326 water. This may contribute to the tentatively lower liquidus reported by Müller et al. (2017).
327 Here, Raman spectroscopy verified the absence of hydrous phases in all run products.
328 Furthermore, impurities can reduce the melting point. The total content of trace elements in
329 the starting mixtures was <1 wt%. Thus, a quasi-ideal behavior and consequently minor
330 affect on the phase relations is assumed. Redox conditions may affect phase relations and
331 carbonate melting (Foley 2011). Although redox conditions were not controlled, the choice of
332 graphite as heater in combination with Pt-capsules (this study and Müller et al. (2017)) and
333 graphite as capsule material (Shatskiy et al. 2018) might have established redox conditions
334 close to the CCO buffer.

335 Our experimentally obtained liquidus is confirmed by thermodynamic modelling of the
336 CaCO_3 - MgCO_3 system (Figure 4b). The computed and experimentally obtained
337 compositions of solid carbonates and carbonate melt correlate within a derivation of $<8\%$ for
338 Mg-rich bulk compositions (Table 1). Modeled, subsolidus phase relation for Ca-rich
339 compositions might be affected by the reaction of aragonite and magnesite to dolomite for
340 temperatures ≥ 1000 °C at 6 GPa (Buob et al. 2006; Franzolin et al. 2011). This reaction is
341 not considered in the thermodynamic modeling, because the used solid solution model for

342 carbonates from Franzolin et al. (2011) was calibrated based on experiments performed at
343 pressures ≤ 3.5 GPa. Consequently, the model may misleadingly predict aragonite at ~ 1300 -
344 1500 °C, whereby aragonite was not observed at 6 GPa.

345 **Figure 4**

346 **Trace element partitioning**

347 Ca-Mg-carbonates can contain variable amounts of Li, K, Na, Mn, Fe, Ba, Sr, Pb and REEs
348 (Dawson and Hinton 2003; Ionov and Harmer 2002; Ionov et al. 1996). Partial melting of
349 carbonates will enrich some trace elements in the melt. Complementary, crystallization of
350 carbonates from a CO₂-rich melt will sequester trace elements compatible in newly formed
351 carbonates. Thus, the partition coefficients between calcite and dolomitic melt at
352 1350 - 1442 °C (Figure 5a), magnesite and dolomitic melt at 1600 °C (Figure 5b) and
353 Ca-magnesite and dolomitic melt at 1400 °C (Figure 5b) were established at 6 GPa. The
354 investigated range in bulk X_{Mg} and temperature enables to discuss the incorporation of trace
355 elements in context of different X_{Mg} , temperature and carbonate structure ($R\bar{3}c$ for magnesite
356 versus $R\bar{3}m$ for calcite at the investigated PT-conditions; Fiquet et al. (1994); Ishizawa
357 (2014)). In the presence of magnesite, single charged cations are strongly enriched in the melt
358 and the concentrations of Li, Na and K in magnesite are below the LA-ICP-MS detection
359 limits (Table 2). Calcite, in contrast, can incorporate to some extent single charged cations
360 and Na⁺, with an ionic radii similar to Ca²⁺, is with $D \sim 0.1 - 0.3$ slightly more compatible
361 than Li⁺ ($0.03 \leq D \leq 0.07$) and K⁺ ($0.1 \leq D \leq 0.24$) (Figure S1a and S1b in the supplementary
362 information). Also, the partition coefficients of divalent cations between calcite and dolomitic
363 melt increase in a parabolic trend as their size of the cations approaches the radius of Ca²⁺
364 (Figure S1a-b). For instance, the partition coefficient between calcite and dolomitic melt
365 (run A and B) decreases from Sr²⁺ to Ba²⁺ (Table 2, Figure S1a-b). Therefore, the partitioning
366 of divalent cations into calcite seems to follow lattice constraints (as employed by Blundy

367 and Wood (2003); Goldschmidt (1937)). Also, the distribution of divalent cations into
368 magnesite seems to follow lattice constraints: the larger the difference between the radii of a
369 particular cation to the size of Mg^{2+} , the lower the partition coefficient between magnesite
370 and dolomitic melt and thus $D(Sr^{2+}) > D(Ba^{2+})$ (Figure S1c-d). Increasing Ca-content in
371 magnesite and decreasing temperature enhance the incorporation of cations with a radius
372 similar or larger to Ca^{2+} like Ba^{2+} , Sr^{2+} and LREEs³⁺ (Figure S1c-d). For instance, partition
373 coefficients of Sr and Ba between Ca-magnesite ($X_{Mg}=0.89$) and dolomitic melt ($X_{Mg}=0.5$) at
374 1400 °C (run D) are ~10 to ~1000 times larger than between magnesite ($X_{Mg}=0.96$) and
375 dolomitic melt ($X_{Mg}=0.8$) at 1600 °C (run C). Also LREEs become more compatible as the
376 Ca-content in magnesite increase (and temperature decreases). The partition coefficients of Y
377 and REEs between magnesite ($X_{Mg}=0.96$) and dolomitic melt ($X_{Mg}=0.8$) range from ~0.001
378 to 0.1 for LREEs to HREEs at 1600 °C (run C). In contrast, partition coefficients of REEs, Sr,
379 Ba, Nb and Y between Ca-richer magnesite ($X_{Mg}=0.89$) and dolomitic melt ($X_{Mg}\sim 0.5$) are
380 more uniform scattering marginal between 0.1 and 0.2 at ~1400 °C (run D) (Figure 5b).

381 **Figure 5**

382 **Implications**

383 This study shows that Ca-Mg-carbonates with X_{Mg} ranging from 0.2 to 0.85 will (partially)
384 melt at 6 GPa and temperatures above ~1300 °C producing a dolomitic melt. Consequently,
385 CO_2 will be liberated by partial melting of an upwelling carbonated mantle at a depth of
386 ~200 km considering the thermal structure of the upper mantle (Ita and Stixrude 1992;
387 McKenzie et al. 2005). The results also affirm that, in the absence of water, carbonates will
388 be stable in the subducting slab even for hot subduction zone geotherms (Syracuse et al.
389 2010).

390 Low-degree melting of carbonated peridotite and carbonated eclogite in the mantle produces
391 a CO_2 -rich liquid (Brey et al. 2008; Dalton and Presnall 1998; Dasgupta and Hirschmann

2006; Dasgupta et al. 2004; Foley et al. 2009; Yaxley and Green 1994; Yaxley and Brey
2004). The onset and composition of the incipient melt is influenced by the melt relations of
the $\text{CaCO}_3\text{-MgCO}_3$ -system, as comparisons between the pure carbonate and carbonated, low-
alkali silicate systems have shown (Buob 2003; Buob et al. 2006; Shatskiy et al. 2018). This
similarity suggests that decisive information like melting temperature and composition
obtained from the pure Ca-Mg-carbonate system can be extrapolated, to some extent, to
chemically more complex systems (containing Si, Al and minor amounts of K and Na) like
carbonated peridotites and carbonated eclogites. This similarity in the major element
composition (X_{Mg}) of a melt produced in the pure $\text{CaCO}_3\text{-MgCO}_3$ -system versus a melt
produced by low-degree melting of a carbonated, low-alkali silicates raises the question, to
which extent also the trace element signature of the incipient melt is influenced by the pure
carbonate system. Green et al. (1992) reported partition coefficients for a sodic, dolomitic
carbonatite magma coexisting with a pargasite-augite-garnet-carbonate assemblage at
2.5 GPa and 1000 °C. X_{Mg} of the carbonatite magma and carbonate crystals is ~0.46 and
~0.43, respectively (Green et al. 1992; Wallace and Green 1988). Although carbonates
($X_{\text{Mg}}=0.14\text{-}0.19$) and dolomitic melt ($X_{\text{Mg}}\sim 0.3$) in experiments performed with CM2 are
Ca-richer, the partition coefficients for REEs and Sr correlate well (Figure 5a). This
observation implies that the REEs and Sr signature of incipient melts of a SiO_2 -bearing
carbonated system can be approximated by the pure carbonate system.

Increasing Ca-content and decreasing temperature enhance the compatibility of Sr, Ba and
LREEs into magnesite (Figure 5b). The compatibility of magnesite for Y and REEs seems
further to be affected by the mineral assemblage. For instance, Dasgupta et al. (2009)
reported partition coefficients between a magnesite-garnet-lherzolite assemblage and
carbonatitic melt at 6.6 GPa and 1265-1300 °C. X_{Mg} of magnesite (0.9 ± 0.03) and dolomitic
melt (0.41 ± 0.05) from the experimental study of Dasgupta et al. (2009) are approximated by

417 run D performed at similar PT-conditions (6 GPa and 1400 °C). Nevertheless, the trace
418 element distribution into magnesite differs (Figure 5b). A carbonatitic melt in equilibrium
419 with a magnesite-garnet-lherzolite likely shows an enrichment of LREEs over HREEs,
420 whereby in the CaCO₃-MgCO₃-system such fractionation would only be expected for
421 melting at higher temperature (1600 °C) (run C; Figure 5b).

422 **Conclusions**

423 The suprasolidus phase relations of the nominally anhydrous CaCO₃-MgCO₃-system at
424 6 GPa were studied by performing multi-anvil experiments. The results demonstrate that:

425 - (partial) melting of Ca-Mg-carbonates occurs at 6 GPa for temperatures above
426 ~1300 °C. Consequently, carbonates are stable during subduction even for hot
427 subduction zone geotherms (Syracuse et al. 2010) unless carbonate bearing lithologies
428 in the slab are infiltrated by aqueous fluids. Considering the thermal structure of the
429 mantle (Ita and Stixrude 1992; McKenzie et al. 2005), CO₂ will be released by
430 (partial) melting of carbonates during upwelling of a carbonated mantle.

431 - In calcite ($X_{Mg}=0.14-0.19$), Li, Na, K, Sr, Ba, Y and REEs are slightly incompatible
432 with partition coefficients around ~0.1-0.8. Trace element distribution between calcite
433 and dolomitic melt seems to follow lattice constraints for divalent cations.

434 In magnesite ($X_{Mg}=0.89-0.96$), Sr, Ba, Y and REEs become more compatible with
435 increasing Ca-content and decreasing temperature. Partition coefficients of Y and
436 REEs between magnesite ($X_{Mg}=0.96$) and dolomitic melt ($X_{Mg}=0.8$) range from
437 ~0.001 to 0.1 for LREEs to HREEs at 1600 °C. In comparison, partition coefficients
438 of REEs, Sr, Ba, Nb and Y between Ca-magnesite ($X_{Mg}=0.89$) and dolomitic melt
439 ($X_{Mg}=0.5$) are more uniform scattering marginal between ~0.1 and 0.2 at ~1400 °C.

440
441
442
443
444
445

446
447
448
449
450
451
452
453
454
455
456
457
458
459
460
461
462
463
464
465
466
467
468
469
470
471
472
473
474
475
476
477
478
479
480
481
482
483
484
485
486
487
488
489
490
491
492
493
494

Acknowledgments

We are grateful to A. Ebert, O. Appelt and C. Wohlgemuth-Überwasser for their assistance in experimental and analytical work. We like to thank A. Shatskiy and an anonymous reviewer for their constructive comments and C. E. Lesher for editorial handling of the paper. This study was funded by the DFG funded research group FOR2125 CarboPaT under the grant number KO1260/19-1.

References

- Alt, J. C., and Teagle, D. A. (1999) The uptake of carbon during alteration of ocean crust. *Geochimica et Cosmochimica Acta*, 63, 1527-1535.
- Blundy, J., and Wood, B. (2003) Partitioning of trace elements between crystals and melts. *Earth and Planetary Science Letters*, 210, 383-397.
- Brey, G. P., Bulatov, V. K., Gurnis, A. V., and Lahaye, Y. (2008) Experimental melting of carbonated peridotite at 6-10 GPa. *Journal of Petrology*, 49, 797-821.
- Buob, A. (2003) The System CaCO₃-MgCO₃: Experiments and Thermodynamic Modeling of the Trigonal and Orthorhombic Solid Solutions at High Pressure and Temperature: PhD thesis.
- Buob, A., Schmidt, M. W., Ulmer, P., and Luth, R. W. (2006) Experiments on CaCO₃-MgCO₃ solid solutions at high pressure and temperature. *American Mineralogist*, 91, 435-440.
- Connolly, J. A. D. (2005) Computation of phase equilibria by linear programming: A tool for geodynamic modeling and its application to subduction zone decarbonation. *Earth and Planetary Science Letters*, 236, 524-541.
- Dalton, J. A., and Wood, B. J. (1993) The compositions of primary carbonate melts and their evolution through wallrock reaction in the mantle. *Earth and Planetary Science Letters*, 119, 511-525.
- Dalton, J. A., and Presnall, D. C. (1998) The Continuum of Primary Carbonatitic-Kimberlitic Melt Compositions in Equilibrium with Lherzolite: Data from the System CaO-MgO-Al₂O₃-SiO₂-CO₂ at 6 GPa. *Journal of Petrology*, 39, 1953-1964.
- Dasgupta, R., and Hirschmann, M. M. (2006) Melting in the Earth's deep upper mantle caused by carbon dioxide. *Nature*, 440, 659.
- Dasgupta, R., and Hirschmann, M. M. (2010) The deep carbon cycle and melting in Earth's interior. *Earth and Planetary Science Letters*, 298, 1-13.
- Dasgupta, R., Hirschmann, M. M., and Withers, A. C. (2004) Deep global cycling of carbon constrained by the solidus of anhydrous, carbonated eclogite under upper mantle conditions. *Earth and Planetary Science Letters*, 227, 73-85.
- Dasgupta, R., Hirschmann, M. M., McDonough, W. F., Spiegelman, M., and Withers, A. C. (2009) Trace element partitioning between garnet lherzolite and carbonatite at 6.6 and 8.6 GPa with applications to the geochemistry of the mantle and of mantle-derived melts. *Chemical Geology*, 262, 57-77.
- Dawson, J., and Hinton, R. (2003) Trace-element content and partitioning in calcite, dolomite and apatite in carbonatite, Phalaborwa, South Africa. *Mineralogical Magazine*, 67, 921-930.
- Deon, F., Koch-Müller, M., Rhede, D., and Wirth, R. (2011) Water and Iron effect on the P-T-x coordinates of the 410-km discontinuity in the Earth upper mantle. *Contributions to Mineralogy and Petrology*, 161, 653-666.
- Fiquet, G., Guyot, F., and Itie, J.-P. (1994) High-pressure X-ray diffraction study of carbonates: MgCO₃, CaMg(CO₃)₂, and CaCO₃. *American Mineralogist*, 79, 15-23.
- Foley, S. F. (2011) A Reappraisal of Redox Melting in the Earth's Mantle as a Function of Tectonic Setting and Time. *Journal of Petrology*, 52, 1363-1391.
- Foley, S. F., Yaxley, G. M., Rosenthal, A., Buhre, S., Kiseeva, E. S., Rapp, R. P., and Jacob, D. E. (2009) The composition of near-solidus melts of peridotite in the presence of CO₂ and H₂O between 40 and 60 kbar. *Lithos*, 112, 274-283.
- Franzolin, E., Schmidt, M. W., and Poli, S. (2011) Ternary Ca-Fe-Mg carbonates: subsolidus phase relations at 3.5 GPa and a thermodynamic solid solution model including order/disorder. *Contributions to Mineralogy and Petrology*, 161, 213-227.
- Gaillard, F., Malki, M., Iacono-Marziano, G., Pichavant, M., and Scaillet, B. J. S. (2008) Carbonatite melts and electrical conductivity in the asthenosphere, 322, 1363-1365.
- Geological-Society-London, 2011: Rare Earth Elements A briefing note by the Geological Society of London. December 2011 ed.
- Goldschmidt, V. M. (1937) The principles of distribution of chemical elements in minerals and rocks. The seventh Hugo Müller Lecture, delivered before the Chemical Society on March 17th, 1937. *Journal of the Chemical Society (Resumed)*, 655-673.
- Gorman, P. J., Kerrick, D. M., and Connolly, J. A. D. (2006) Modeling open system metamorphic decarbonation of subducting slabs. *Geochemistry, Geophysics, Geosystems*, 7, n/a-n/a.

495 Green, T. H., Adam, J., and Siel, S. H. (1992) Trace element partitioning between silicate minerals and carbonatite at 25
496 kbar and application to mantle metasomatism. *Mineralogy and Petrology*, 46, 179-184.

497 Hazen, R. M., Jones, A. P., and Baross, J. A., 2013: Carbon in earth. Vol. 75.

498 Hirschmann, M. M. (2000) Mantle solidus: Experimental constraints and the effects of peridotite composition.
499 *Geochemistry, Geophysics, Geosystems*, 1.

500 Holland, T. J. B., and Powell, R. (1998) An internally consistent thermodynamic data set for phases of petrological interest.
501 *Journal of Metamorphic Geology*, 16, 309-343.

502 Hunter, R. H., and McKenzie, D. (1989) The equilibrium geometry of carbonate melts in rocks of mantle composition.
503 *Earth and Planetary Science Letters*, 92, 347-356.

504 Ionov, D., and Harmer, R. E. (2002) Trace element distribution in calcite–dolomite carbonatites from Spitskop: inferences
505 for differentiation of carbonatite magmas and the origin of carbonates in mantle xenoliths. *Earth and Planetary Science*
506 *Letters*, 198, 495-510.

507 Ionov, D. A., Dupuy, C., O'Reilly, S. Y., Kopylova, M. G., and Genshaft, Y. S. (1993) Carbonated peridotite xenoliths from
508 Spitsbergen: implications for trace element signature of mantle carbonate metasomatism. *Earth and Planetary Science*
509 *Letters*, 119, 283-297.

510 Ionov, D. A., O'Reilly, S. Y., Genshaft, Y. S., Kopylova, M. G. J. C. t. M., and Petrology (1996) Carbonate-bearing mantle
511 peridotite xenoliths from Spitsbergen: phase relationships, mineral compositions and trace-element residence, 125, 375-392.

512 Ishizawa, N. (2014) Calcite V: a hundred-year-old mystery has been solved. *Powder Diffraction*, 29, S19-S23.

513 Ita, J., and Stixrude, L. (1992) Petrology, elasticity, and composition of the mantle transition zone. *Journal of Geophysical*
514 *Research: Solid Earth*, 97, 6849-6866.

515 Jochum, K. P., Weis, U., Stoll, B., Kuzmin, D., Yang, Q., Raczek, I., Jacob, D. E., Stracke, A., Birbaum, K., Frick, D. A.,
516 Günther, D., and Enzweiler, J. (2011) Determination of Reference Values for NIST SRM 610–617 Glasses Following ISO
517 Guidelines. *Geostandards and Geoanalytical Research*, 35, 397-429.

518 Kelemen, P. B., and Manning, C. E. (2015) Reevaluating carbon fluxes in subduction zones, what goes down, mostly comes
519 up. *Proceedings of the National Academy of Sciences USA*, 112, E3997-4006.

520 Keppler, H. (2003) Water solubility in carbonatite melts. *American Mineralogist*, 88, 1822-1824.

521 Kerrick, D. M., and Connolly, J. A. D. (1998) Subduction of ophicarbonates and recycling of CO₂ and H₂O. *Geology*, 26,
522 375-378.

523 Kerrick, D. M., and Connolly, J. A. D. (2001) Metamorphic devolatilization of subducted oceanic metabasalts: implications
524 for seismicity, arc magmatism and volatile recycling. *Earth and Planetary Science Letters*, 189, 19-29.

525 Korsakov, A. V., and Hermann, J. (2006) Silicate and carbonate melt inclusions associated with diamonds in deeply
526 subducted carbonate rocks. *Earth and Planetary Science Letters*, 241, 104-118.

527 Kruk, A. N., Sokol, A. G., and Palyanov, Y. N. J. P. (2018) Phase Relations in the Harzburgite–Hydrous Carbonate Melt at
528 5.5–7.5 GPa and 1200–1350°C, 26, 575-587.

529 McKenzie, D., Jackson, J., and Priestley, K. (2005) Thermal structure of oceanic and continental lithosphere. *Earth and*
530 *Planetary Science Letters*, 233, 337-349.

531 Müller, J., Koch-Müller, M., Rhede, D., Wilke, F. D., and Wirth, R. (2017) Melting relations in the system CaCO₃-MgCO₃
532 at 6 GPa. *American Mineralogist: Journal of Earth and Planetary Materials*, 102, 2440-2449.

533 Piccoli, F., Vitale Brovarone, A., Beyssac, O., Martinez, I., Ague, J. J., and Chaduteau, C. (2016) Carbonation by fluid–rock
534 interactions at high-pressure conditions: Implications for carbon cycling in subduction zones. *Earth and Planetary Science*
535 *Letters*, 445, 146-159.

536 Scambelluri, M., Bebout, G. E., Belmonte, D., Gilio, M., Campomenosi, N., Collins, N., and Crispini, L. (2016)
537 Carbonation of subduction-zone serpentinite (high-pressure ophicarbonate; Ligurian Western Alps) and implications for the
538 deep carbon cycling. *Earth and Planetary Science Letters*, 441, 155-166.

539 Schmidt, M. W., and Ulmer, P. (2004) A rocking multianvil: elimination of chemical segregation in fluid-saturated high-
540 pressure experiments. *Geochimica et Cosmochimica Acta*, 68, 1889-1899.

541 Shannon, R., and Prewitt, C. (1970) Revised values of effective ionic radii. *Acta Crystallographica Section B: Structural*
542 *Crystallography and Crystal Chemistry*, 26, 1046-1048.

543 Shannon, R. T., and Prewitt, C. T. (1969) Effective ionic radii in oxides and fluorides. *Acta Crystallographica Section B:*
544 *Structural Crystallography and Crystal Chemistry*, 25, 925-946.

545 Shatskiy, A., Podborodnikov, I. V., Arefiev, A. V., Minin, D. A., Chanyshv, A. D., and Litasov, K. D. (2018) Revision of
546 the CaCO₃–MgCO₃ phase diagram at 3 and 6 GPa. *American Mineralogist*, 103, 441-452.

547 Shatsky, V., Ragozin, A., and Sobolev, N. (2006) Some aspects of metamorphic evolution of ultrahigh-pressure calc-silicate
548 rocks of the Kokchetav Massif. *Russian Geology and Geophysics (Geologiya i Geofizika)*, 47, 105-119.

549 Sieber, M. J., Hermann, J., and Yaxley, G. M. (2018) An experimental investigation of C-O-H fluid-driven carbonation of
550 serpentinites under forearc conditions. *Earth and Planetary Science Letters*, 496, 177-188.

551 Stachel, T., and Harris, J. W. (2008) The origin of cratonic diamonds — Constraints from mineral inclusions. *Ore Geology*
552 *Reviews*, 34, 5-32.

553 Syracuse, E. M., van Keken, P. E., and Abers, G. A. (2010) The global range of subduction zone thermal models. *Physics of*
554 *the Earth and Planetary Interiors*, 183, 73-90.

555 Vernon, R. H., 2004: A Practical Guide to Rock Microstructure. 2 ed. Vol. 1, Cambridge University Press.

556 Wallace, M. E., and Green, D. H. (1988) An experimental determination of primary carbonatite magma composition.
557 *Nature*, 335, 343-346.

558 Walter, M. J., Thibault, Y., Wei, K., and Luth, R. W. (1995) Characterizing experimental pressure and temperature
559 conditions in multi-anvil apparatus. *Canadian Journal of Physics*, 73, 273-286.

560 Wang, A., Pasteris, J. D., Meyer, H. O. A., and Dele-Duboi, M. L. (1996) Magnesite-bearing inclusion assemblage in
561 natural diamond. *Earth and Planetary Science Letters*, 141, 293-306.

562 Watenphul, A., Wunder, B., and Heinrich, W. (2009) High-pressure ammonium-bearing silicates: Implications for nitrogen
563 and hydrogen storage in the Earth's mantle. *American Mineralogist*, 94, 283-292.
564 Yaxley, G. M., and Green, D. H. (1994) Experimental demonstration of refractory carbonate-bearing eclogite and siliceous
565 melt in the subduction regime. *Earth and Planetary Science Letters*, 128, 313-325.
566 Yaxley, G. M., and Brey, G. P. (2004) Phase relations of carbonate-bearing eclogite assemblages from 2.5 to 5.5 GPa:
567 implications for petrogenesis of carbonatites. *Contributions to Mineralogy and Petrology*, 146, 606-619.
568 Zhang, X., Yang, S.-Y., Zhao, H., Jiang, S.-Y., Zhang, R.-X., and Xia, J. (2017) Effect of beam current and diameter on
569 electron probe microanalysis of carbonate minerals. *Journal of Earth Science*.
570

571 **Tables caption**

572 Table 1: Overview of the performed experiments. Two starting mixtures (CM1 and CM2)
573 with a bulk X_{Mg} of 0.85 and 0.2 were used. In all experiments, liquid and solid carbonate
574 phase were present under high pressures (6 GPa) and temperatures (T). Calculations of phase
575 proportions are based on geometric constraints (e.g. observations from BSE-images) and
576 computed densities of solid carbonates (see text for more details).

577

578 Table 2: Trace element concentration of carbonate crystals and carbonate melt and partition
579 coefficient (D). The trace element composition of the melt in run D is calculated per
580 mass-balance. All other concentrations are determined by LA-ICP-MS.

581 **Figure caption**

582 Figure 1: BSE-images of recovered capsules: (a, e) run A; (b, f) run B; (c, g) run C; (d, h)
583 run D. In all experiments, a carbonate melt (liq) and solid carbonates (carb) are present. In
584 run A small amounts of periclase (per) were observed.

585

586 Figure 2: The Sr (left) and Ba (right) composition of solid carbonates and carbonate melt
587 were measured by EPMA-WDS (abscissa). The microprobe results correlate well with
588 LA-ICP-MS measurements (ordinate) of carbonate crystals (diamonds) and melts (dark-gray
589 circles). Mass-balance calculations (ordinate) also constrained the trace element compositions
590 of the melts (light-gray circles). Within the uncertainties, the measured and calculated

591 compositions correlate well testifying the applicability of the mass-balance approach to
592 calculate the trace element composition of the melt.

593

594 Figure 3: Trace element compositions of carbonate crystals (white symbols) and carbonate
595 melts (red symbols) per LA-ICP-MS normalized to the start mixtures (CM1 and CM2).
596 LILEs, Nb, Y and REEs are enriched in the melts. Relative to the start mixtures, Fe, Mn, Pb,
597 Pr, Gd and Tb are depleted in carbonate crystals and carbonate melts indicating alloy
598 formation with the Pt capsule.

599

600 Figure 4: The here observed suprasolidus phase relations of the $\text{CaCO}_3\text{-MgCO}_3$ -system at
601 6 GPa (black, thick curves and black, bold labels) are compared to (a) the experimental
602 studies of Shatskiy et al. (2018) (green, thin curves and green, italic labels) and Müller et al.
603 (2017) (blue, thin curves). In (b) our results are compared to thermodynamical modelled
604 phase relations (orange, thin curves and orange, italic labels). The model may misleadingly
605 predict aragonite at $\sim 1300\text{-}1500\text{ }^\circ\text{C}$, because the reaction of aragonite and magnesite to
606 dolomite is not considered in the solid solution model (details in text). The median
607 composition of carbonate melts (gray circles) and carbonate crystals (open diamonds) per
608 EPMA-WDS is plotted and the error bars represents the data range without outlier rejection.

609

610 Figure 5: Partition coefficients (D) between (a) calcite and dolomitic melt (run A and B) and
611 (b) magnesite and dolomitic melt (run C and D). The legend lists the starting mixtures (CM1,
612 CM2), the temperature [$^\circ\text{C}$] and X_{Mg} of solid carbonates and melts.

613

Supplementary

614 Figure S1: Partition coefficient (D) as a function of charge and ionic radius for (a) run A, (b)
615 run B, (c) run C and (d) run D. Straight, solid lines refer to the 6-fold coordinated ionic radii

616 of Mg^{2+} (0.072 nm) and Ca^{2+} (0.1 nm) (Shannon and Prewitt 1970; Shannon and Prewitt
617 1969).

experimental conditions				observed phase	calculated proportion [wt%]	composition per FE-EPMA			per thermodynamic modelling			
run	T [°C]	start-mix	bulk X_{Mg}			X_{Mg} min	X_{Mg} average	X_{Mg} max	modelled phase	density [g/cm ³]	proportion [wt%]	X_{Mg}
A	1442	CM2	0,2	melt	32	0,29	0,31	0,32	melt		64	0,31
				calcite	68	0,10	0,14	0,17	aragonite	2,88	36	0,0
				periclase	uc						\	
B	1350	CM2	0,2	melt	6	0,30	0,33	0,36	melt		21	0,37
				calcite	94	0,17	0,19	0,21	carbonate	2,84	79	0,15
				calcite II	uc	0,20	0,28	0,32			\	
C	1600	CM1	0,85	melt	92	0,78	0,80	0,82	melt		95	0,84
				magnesite	8	0,96	0,96	0,97	carbonate	2,96	5	0,999
D	1400	CM1	0,85	melt	14	0,38	0,50	0,61	melt		26	0,53
				Ca-magnesite	86	0,87	0,89	0,91	carbonate	2,97	74	0,95

uc unconstrained

	Run A (melt composition per LA-ICP-MS)			Run B (melt composition per LA-ICP-MS)			Run C (melt composition per LA-ICP-MS)			Run D (melt composition per LA-ICP-MS)			Run D (melt composition per mass balance)		
	calcite $X_{Mg}=0.14$ [ppm]	Melt $X_{Mg}=0.31$ [ppm]	D	calcite $X_{Mg}=0.19$ [ppm]	Melt $X_{Mg}=0.33$ [ppm]	D	magnesite $X_{Mg}=0.96$ [ppm]	Melt $X_{Mg}=0.8$ [ppm]	D	Ca-magnesite $X_{Mg}=0.89$ [ppm]	Melt $X_{Mg}=0.5$ [ppm]	D	Ca-magnesite $X_{Mg}=0.89$ [ppm]	Melt $X_{Mg}=0.5$ [ppm]	D
Li	2	51	0,03	5	77	0,07	<dl	30		<dl	179		<dl		
2σ	1	5	0,02	4	24	0,05		2			79				
Na	33	241	0,14	91	352	0,3	<dl	373		<dl	<dl		<dl		
2σ	20	36	0,08	46	105	0,2		48							
K	29	292	0,10	66	275	0,24	<dl	126		<dl	<dl		<dl		
2σ	10	38	0,04	10	86	0,08		15							
Mn	19	9		43	262		201	170		<dl	320		<dl		
2σ	15	1		8	32		10	7			135				
Fe	428	384		556	7069		260	175		<dl	995		<dl		
2σ	105	64		476	3434		15	32			645				
Sr	150	239	0,63	195	233	0,8	3	294	0,009	119	905	0,13	119	1481	0,10
2σ	12	6	0,05	40	11	0,2	0	7	0,001	53	138	0,06	53		
Y	117	344	0,3	119	427	0,28	13	319	0,042	126	658	0,19	126	1086	0,14
2σ	67	10	0,2	22	30	0,05	1	9	0,003	46	95	0,07	46		
Nb	0,3	537	0,0006	2,0	981	####	<dl	257		75	297	0,25	75	1351	0,07
2σ	0,2	36	0,0004	2,3	269	####		10		126	75	0,43	126		
Ba	90	664	0,14	165	634	0,26	0,0	418	0,0001	150	995	0,15	150	3164	0,06
2σ	30	25	0,05	27	140	0,07	0,8	24	0,0018	81	185	0,09	81		
La	132	745	0,2	153	909	0,17	0,7	528	0,0014	159	1305	0,12	159	1983	0,10
2σ	90	11	0,1	22	157	0,04	0,2	22	0,0004	59	210	0,05	59		
Ce	139	752	0,2	155	1195	0,13	1,4	537	0,0026	224	1755	0,13	224	1516	0,17
2σ	95	27	0,1	61	241	0,06	0,2	20	0,0004	95	290	0,06	95		
Pr	128	595		148	786		1,1	472		173	1375		173		
2σ	83	14		20	122		0,2	17		95	270		95		
Nd	167	631	0,3	175	790	0,22	2,1	502	0,004	180	1415	0,13	180	1946	0,11
2σ	108	35	0,2	39	86	0,06	0,5	26	0,001	85	260	0,06	85		
Sm	165	584	0,3	181	738	0,24	3,6	489	0,007	176	1205	0,15	176	2117	0,10
2σ	104	27	0,2	40	62	0,06	0,5	11	0,001	93	200	0,08	93		
Eu	193	524	0,4	213	759	0,28	5,2	505	0,010	174	1310	0,13	174	2163	0,10
2σ	81	15	0,2	66	64	0,09	0,6	16	0,001	83	235	0,07	83		
Gd	91	312		101	403		3,6	276		96	693		96		
2σ	55	10		18	38		0,7	7		43	130		43		
Tb	183	606		195	828		11,6	549		209	1335		209		
2σ	110	18		28	100		0,8	19		68	230		68		
Dy	187	615	0,3	209	849	0,25	15,8	536	0,029	199	1170	0,17	199	2220	0,11
2σ	112	19	0,2	32	89	0,05	1,1	12	0,002	55	190	0,05	55		
Ho	204	644	0,3	219	938	0,23	23,1	569	0,041	213	1200	0,18	213	2168	0,12
2σ	119	26	0,2	28	124	0,04	1,3	15	0,002	74	180	0,07	74		
Er	192	582	0,3	202	805	0,25	28,3	539	0,052	222	1115	0,20	222	2151	0,12
2σ	113	15	0,2	20	77	0,03	2,0	12	0,004	87	165	0,08	87		
Tm	215	681	0,3	228	998	0,23	36,4	525	0,069	243	1145	0,21	243	2031	0,14
2σ	121	36	0,2	32	97	0,04	2,2	13	0,005	89	145	0,08	89		
Yb	227	633	0,4	238	918	0,26	48,9	563	0,087	249	1150	0,22	249	2082	0,14
2σ	139	25	0,2	38	77	0,05	2,6	20	0,005	94	165	0,09	94		
Lu	196	581	0,3	225	850	0,26	56,0	497	0,113	239	945	0,25	239	2198	0,13
2σ	111	12	0,2	44	72	0,06	2,8	17	0,007	89	125	0,10	89		
Pb	31	5,3		317	169		0,7	34		7	68		7		
2σ	53	0,4		90	45		0,1	3		3	31		3		

<dl: below detection limit

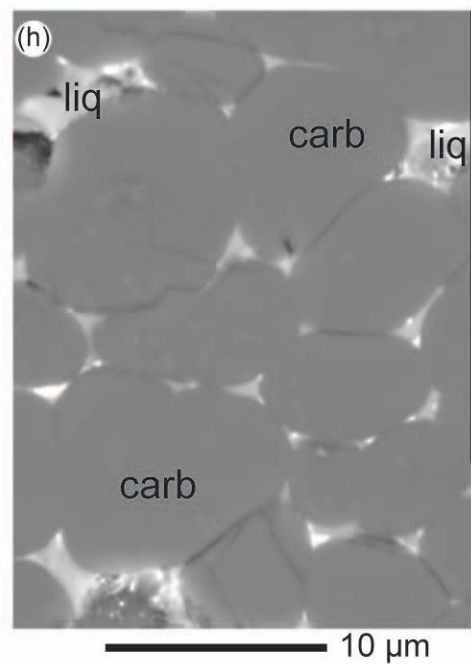
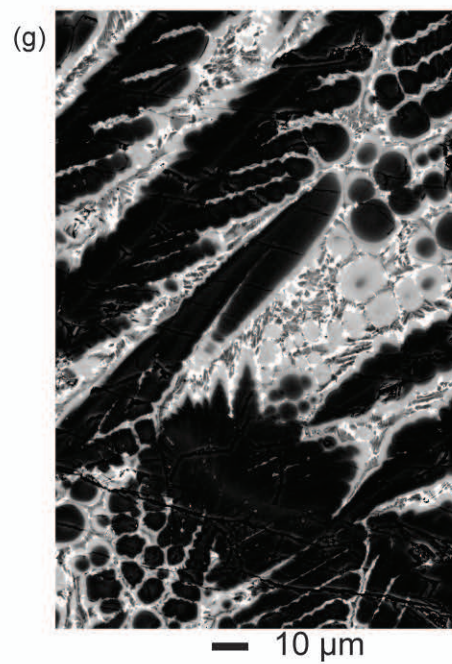
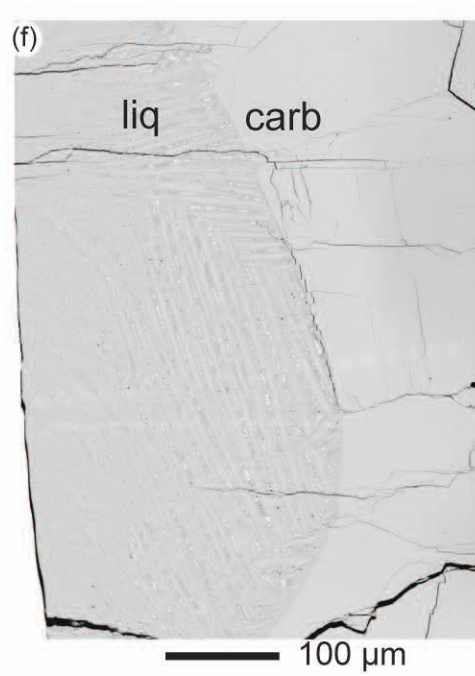
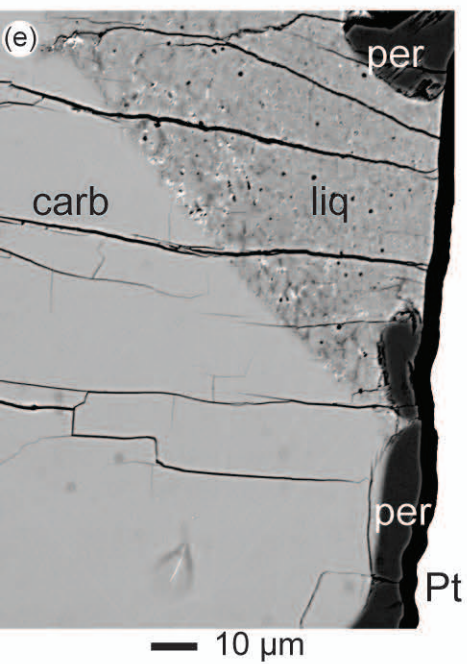
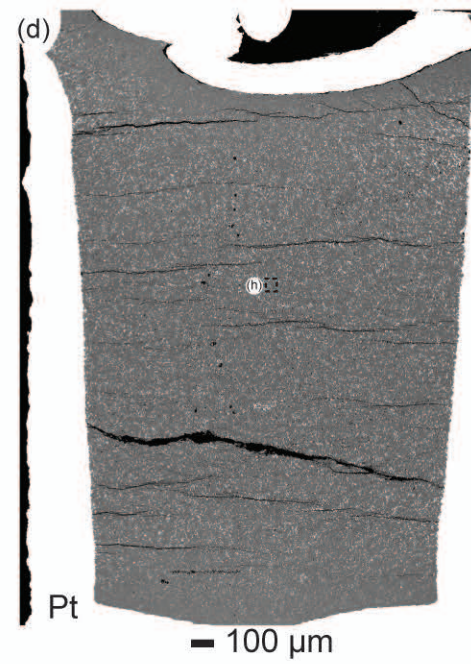
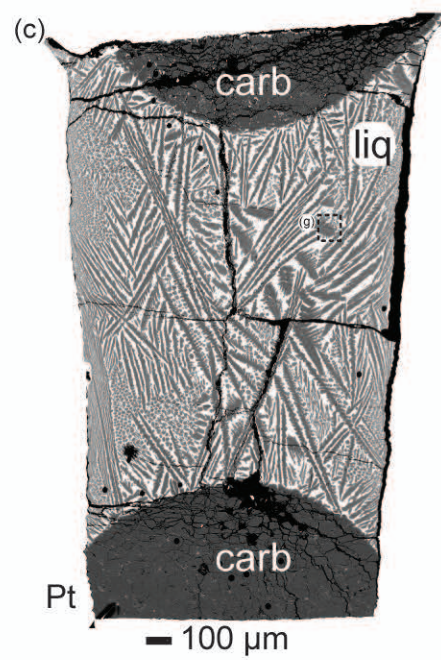
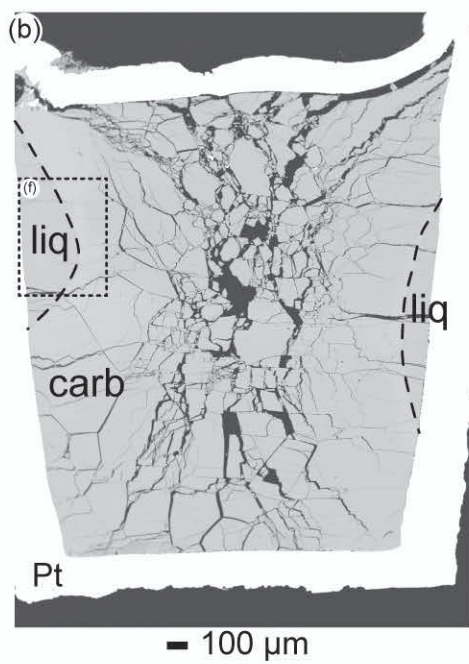
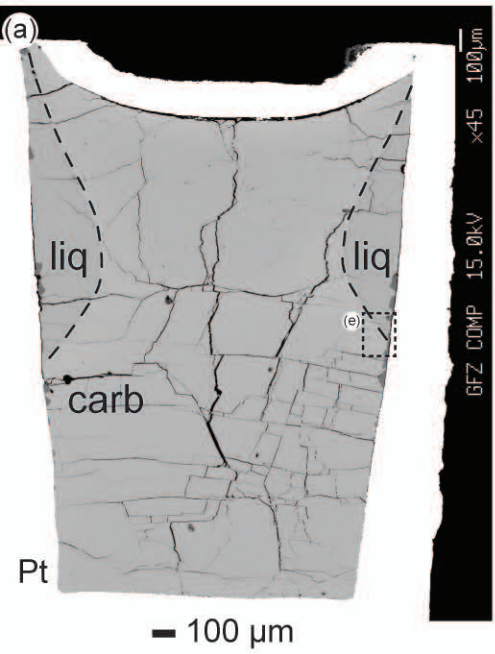
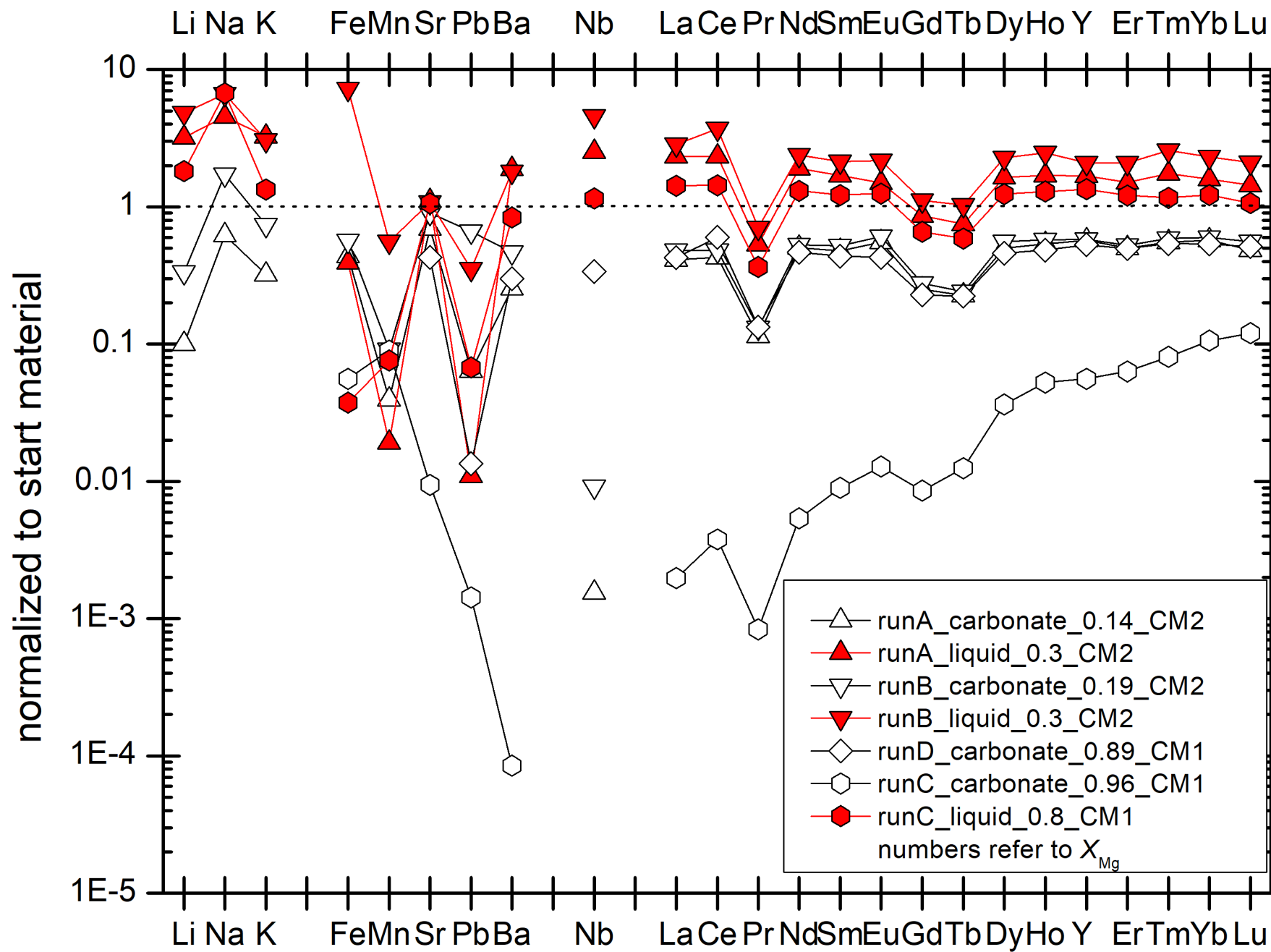


Fig 3



(a)

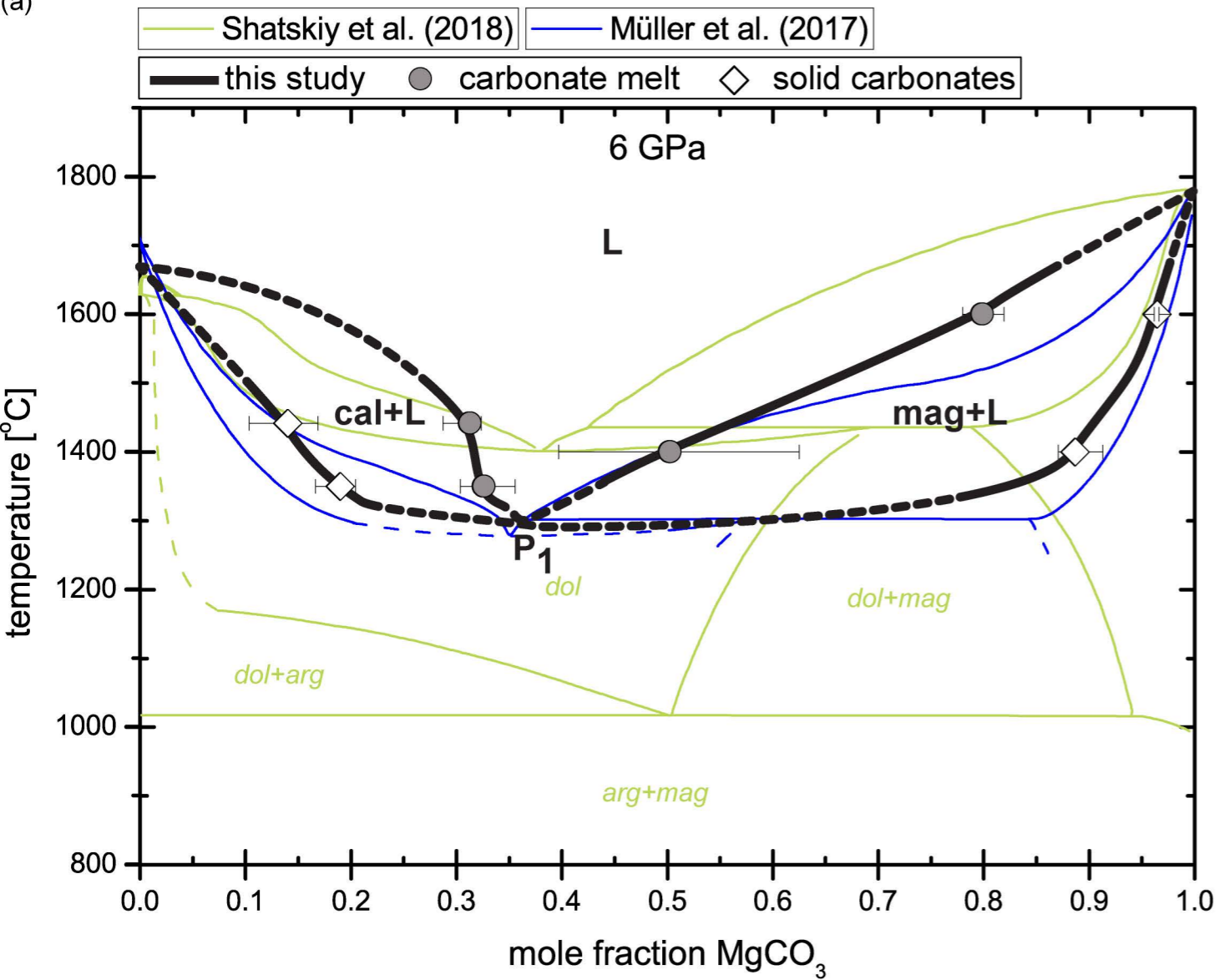
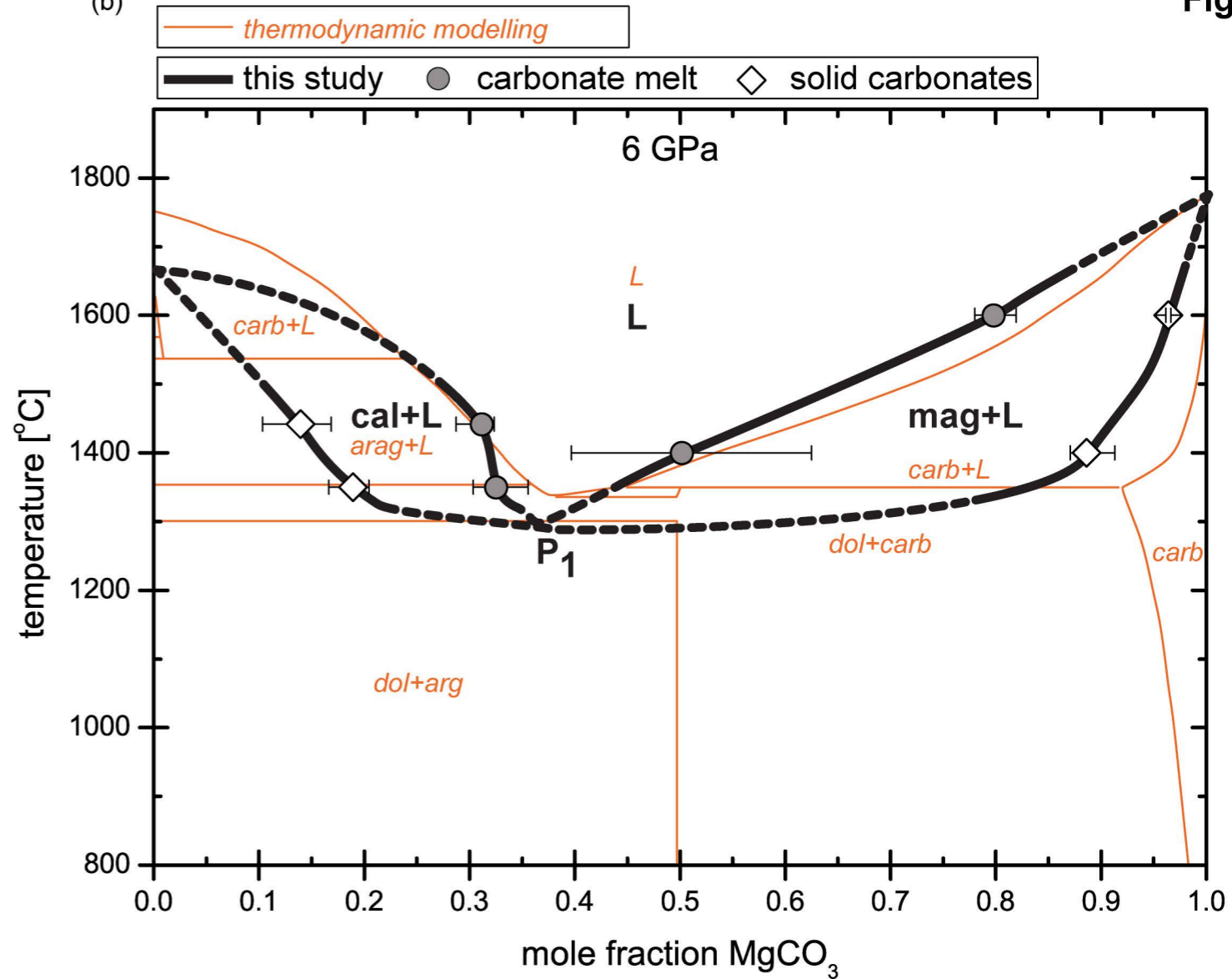
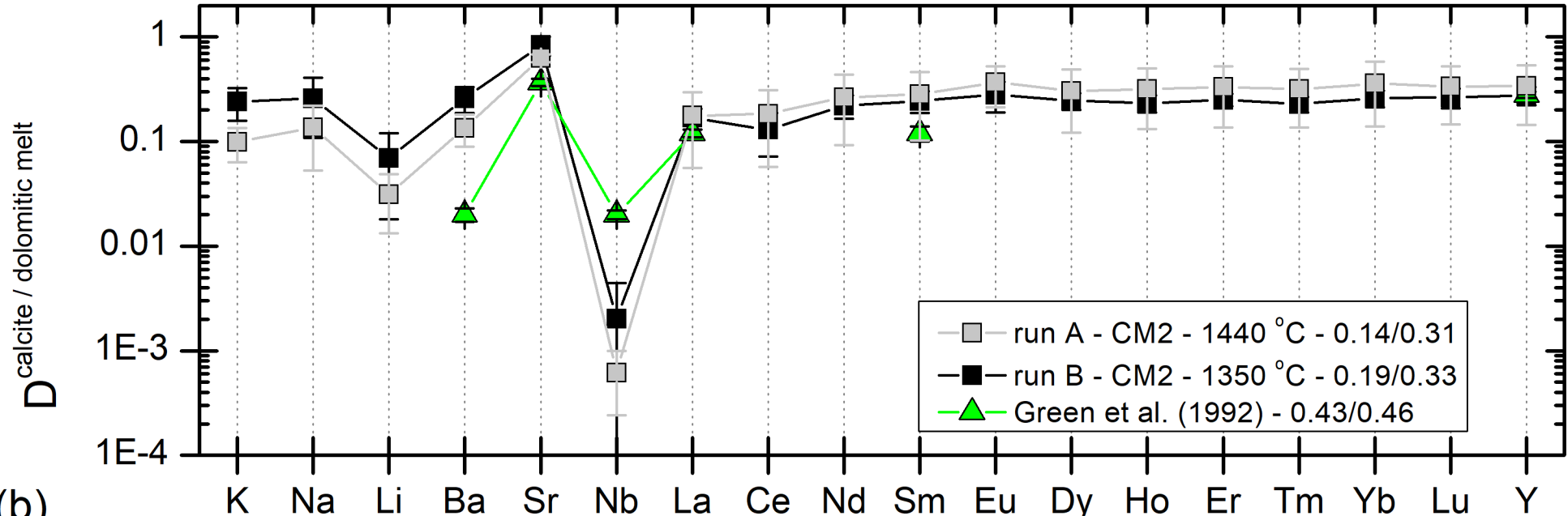


Fig 4

(b)



(a)



(b)

